Measuring transfer functions of track structures in a test rig with laser Doppler vibrometer and accelerometers on a moving vehicle

Zeng, Yuanchen; Núñez, Alfredo; Li, Zili

DOI
10.1016/j.ymssp.2024.111392

Publication date
2024

Document Version
Final published version

Published in
Mechanical Systems and Signal Processing

Mechanical Systems and Signal Processing 214 (2024) 111392

Contents lists available at ScienceDirect

Mechanical Systems and Signal Processing

journal homepage: www.elsevier.com/locate/ymssp

Measuring transfer functions of track structures in a test rig with laser Doppler vibrometer and accelerometers on a moving vehicle

Yuanchen Zeng, Alfredo Núñez, Zili Li *

Section of Railway Engineering, Department of Engineering Structures, Faculty of Civil Engineering and Geosciences, Delft University of Technology, Stevinweg 1, Delft, the Netherlands

ARTICLE INFO

Keywords:
Transfer function
Frequency response function
Railway track structure
Laser Doppler vibrometer
Modal identification
Force estimation

ABSTRACT

A transfer function (TF) is an effective representation of the load-response relationship of railway track structures. To fill the gap in measuring track structure TFs over a wide frequency range from a moving vehicle, we develop a TF measurement system and the associated TF estimation methodology. Accelerometers are utilized to estimate the dynamic vehicle load to track structures, and a laser Doppler vibrometer (LDV) is used to scan track structures and measure their vibration response. First, operational modal analysis is applied to vehicle impact response over joints to identify its modal parameters, which support the estimation of dynamic wheel-rail forces from vehicle vibrations. This combination eliminates the need to pre-define the vehicle stiffness, vehicle damping, and vehicle body mass and enables the vehicle parameters to be updated under operational conditions. Meanwhile, a signal processing method is applied to LDV signals to reduce speckle noise and compensate for the effect of vehicle vibration. Then, a continuous track structure is segmented into distributed sections, and a TF is estimated for each track section using the estimated wheel-rail force as input and the extracted track vibration as output. We validate the methodology in a vehicle-track test rig on different track sections (with or without joints) and at different speeds (from 8 km/h to 16 km/h). The results are further compared with trackside measurements and hammer tests. We demonstrate that the track vibrations extracted from the LDV signals are consistent with those measured by trackside accelerometers. The shapes and resonance frequencies of the estimated TFs are in good agreement with those measured from the hammer tests in the frequency range of 200–800 Hz. The developed system captures differences in the TFs between different track sections, suggesting its potential to be used for structural health monitoring of railway tracks.

1. Introduction

In structural dynamics, a transfer function (TF) or a frequency response function (FRF) generally refers to the frequency-domain relationship between the input and output of a structure [1]. The input is usually the load or excitation applied to the structure, while the output is usually the dynamic response of the structure, such as its displacement, velocity, and acceleration. A TF or FRF enables the dynamic properties of a structure to be characterized over a wide range of frequencies, thus being useful in the design, identification, monitoring, and control of mechanical and civil structures [1].

* Corresponding author.
E-mail address: Z.Li@tudelft.nl (Z. Li).

https://doi.org/10.1016/j.ymssp.2024.111392
Received 27 November 2023; Received in revised form 11 February 2024; Accepted 29 March 2024
Available online 3 April 2024

Railway tracks are important infrastructure to support train traffic with increasing speeds and axle loads. The dynamic properties of track structures are essential for the safety and ride quality of train operations. A TF or FRF of a railway track structure is an effective representation of its dynamic properties, which is often defined in terms of the load on rails as input and the vibration response of rails or sleepers as output [2,3]. It can be used for parameter identification [4,5] and damage detection [6,7] of railway tracks, thus allowing for structural health monitoring and condition-based maintenance of railway tracks. In the literature, there are two main approaches to (partially) measure railway track TFs or FRFs.

- FRFs of railway tracks can be measured through impact modal testing [4–9]. In such a test, impacts are usually generated manually on the railhead by a hammer with a force transducer, and the track response is measured by accelerometers at locations of interest, usually on rails or sleepers. This approach has the advantages of low noise and high repeatability. However, such tests are usually conducted under conditions without train loads, and different frequency ranges require hammers of different weights and tips [4,5]. Meanwhile, this approach is labor-intensive and time-consuming and requires temporary operation shutdown, so it is mostly applied only in hot spots.
- Specialized vehicles can be deployed to excite track structures with a controlled load from an oscillating mass and measure the track response [10,11]. This approach allows the dynamic stiffness (the reciprocal of reacceptance) of railway tracks to be measured on a moving train but only at a single frequency (below 50 Hz [10]) in one run.

There is still a lack of technology for measuring track structure TFs over a wide frequency range from a moving vehicle. The major challenges are summarized below.

(1) Obtain dynamic vehicle loads (input) to track structures. Track structures are loaded by wheels through wheel-rail contact forces, which are broadband in frequency due to irregularities of wheels and tracks. Such loads can be obtained by measurement or estimation. In practice, the instrumentation and calibration of sensors on a vehicle for wheel-rail force measurement are complicated [12,13]. Since static wheel-rail loads are not a major concern for TF estimation, an alternative solution is to estimate dynamic wheel-rail forces from vehicle vibrations. Many methods have been developed on this topic [14–17], most of which require a vehicle model with all parameters known. This may be difficult or expensive to achieve in real life because of changes and degradation of vehicle parameters, such as changes in vehicle body mass due to changes in passenger or good loads and degradation of springs or dampers.
(2) Measure dynamic responses (output) of track structures. Dynamic responses of track structures are usually obtained through vibration measurement. Laser sensing technology enables non-contact structural vibration measurements. For example, a laser Doppler vibrometer (LDV) can measure the vibration velocity of a target based on the Doppler effect [18,19]. An LDV can be mounted on a vehicle to target its laser spot on track structures and directly measure track vibrations as the vehicle moves [20]. In a simulation study [21], train-borne LDVs measure a bridge to identify its mode shapes. In experimental studies [22,23], train-borne LDVs are used to measure railhead to identify rail bending modes and detect welds. However, speckle noise has been reported to be a major source of noise for an LDV that continuously scans structural surfaces, especially at high scanning speeds [19,20]. It appears as random and irregular spikes in the time domain and becomes a noise floor when transformed into the frequency domain. Speckle noise needs to be mitigated to improve the quality of measured responses. Only a few signal processing methods have been proposed to reduce speckle noise for LDV measurements at high scanning speeds [20,24,25].
(3) Estimate track structure TFs with moving load and response. Conventionally, a TF or FRF is defined based on load and response at fixed locations. When measuring track structure TFs from a running vehicle, the locations of both load and response move and the input–output relationship varies. Therefore, proper segmentation is needed to divide a continuous track structure into distributed sections and estimate an average input–output relationship from measurements on each track section. We investigate its feasibility through simulations [26], in which a TF is estimated for each sleeper using the segmented wheel-rail force and sleeper vibration. It is found that the TFs estimated with the moving load and response are close to those from simulated hammer tests at fixed locations. The vehicle speed and sleeper width affect the length of signals measured on each sleeper and further affect the frequency resolution of the estimated TFs. However, this simulation study neglects nonlinear track stiffness, force estimation errors, and measurement noise.

To tackle the above challenges, we develop in this paper a novel track structure TF measurement system on a moving vehicle and validate the associated TF estimation methodology in a vehicle-track test rig. We are not aware of existing research on such a technology. The main contributions of this paper are summarized as follows.

- The system utilizes an LDV on a moving vehicle to scan the track structure and directly measure its vibration. It is combined with accelerometers on the vehicle to estimate the load-response relationship of the track structure, i.e., a TF for each track section using the dynamic wheel-rail force as the input and the track vibration as the output. The system can continuously measure the TFs of the track structure under loaded conditions.
- We combine operational modal identification of a vehicle passing over joints with wheel-rail force estimation from vehicle vibrations, which eliminates the need to pre-define vehicle stiffness, vehicle damping, and vehicle body mass for wheel-rail force estimation and enables the vehicle modal parameters to be updated regularly under operational conditions.

- The proposed methodology is validated in a vehicle-track test rig at different locations (with or without joints) and speeds (8–16 km/h). The extracted track vibration is consistent with trackside accelerometer measurements, and the estimated TFs show good agreement in terms of the shapes and resonance frequencies with the FRFs measured from the hammer tests at 200–800 Hz.

The remainder of this paper is organized as follows. Section 2 presents the methodology for estimating track structure TFs using LDV and accelerometer measurement. Section 3 conducts experiments in the vehicle-track test rig to validate the proposed methodology. Section 4 concludes this paper with an outlook on future research.

2. Methodology

Fig. 1 shows the proposed methodology for estimating track structure TFs using LDV and accelerometer measurement on a moving vehicle. Accelerometers are mounted on the main masses of the vehicle, and the laser spot of the LDV can be targeted at track components of interest, such as rails or sleepers. First, the impact response of the vehicle when passing over a joint is captured from the accelerometer measurement and then used to identify the modal parameters of the vehicle (natural frequencies, damping ratios, mode shape vectors, and modal masses). Based on these parameters, the dynamic wheel-rail force is then estimated from vehicle vibrations during vehicle running, denoted as $w(t)$, with t denoting time. Meanwhile, the vibration of track structures is extracted from the LDV measurement by reducing the speckle noise and compensating for the effect of vehicle vibration, denoted as $u(t)$. Finally, a TF of each track section $H(f)$, with f denoting frequency, is estimated using the segmented wheel-rail force $w(t)$ as input and the segmented track vibration $u(t)$ as output.

2.1. Input: Modal identification and force estimation

The dynamics of a vehicle system (with n degrees of freedom) is usually characterized by the following equation of motion,

$$\mathbf{M}\ddot{\boldsymbol{x}}(t) + \mathbf{K}\boldsymbol{x}(t) + \mathbf{C}\dot{\boldsymbol{x}}(t) = \boldsymbol{w}(t) \tag{1}$$

where $\mathbf{M}$, $\mathbf{K}$, and $\mathbf{C}$ are the mass, stiffness, and damping matrices, respectively; $\boldsymbol{x}(t)$ is the displacement vector; $\boldsymbol{w}(t)$ is the external force vector, including wheel-rail forces. Eq. (1) can be converted to modal coordinate as follows under the assumption of modal damping,

$$\mathbf{M}^*\ddot{\boldsymbol{q}}(t) + \mathbf{K}^*\boldsymbol{q}(t) + \mathbf{C}^*\dot{\boldsymbol{q}}(t) = \boldsymbol{p}(t) \tag{2}$$

where $\mathbf{M}^*$, $\mathbf{K}^*$, and $\mathbf{C}^*$ are the modal mass, stiffness, and damping matrices, respectively; $\boldsymbol{q}(t)$ and $\boldsymbol{p}(t)$ are the modal displacement and force vectors, respectively. From Eq. (1) to Eq. (2), the following transformation holds,

$$\mathbf{M}^* = \mathbf{\Phi}^{\mathrm{T}}\mathbf{M}\mathbf{\Phi} \quad \mathbf{K}^* = \mathbf{\Phi}^{\mathrm{T}}\mathbf{K}\mathbf{\Phi} \quad \mathbf{C}^* = \mathbf{\Phi}^{\mathrm{T}}\mathbf{C}\mathbf{\Phi} \quad \boldsymbol{x} = \mathbf{\Phi}\boldsymbol{q} \quad \boldsymbol{p} = \mathbf{\Phi}^{\mathrm{T}}\boldsymbol{w} \tag{3}$$

where $\mathbf{\Phi}$ is the mode shape matrix, consisting of mode shape vectors $\varphi_1, \ldots, \varphi_n$, and $\mathbf{M}^*$, $\mathbf{K}^*$, $\mathbf{C}^*$ are diagonal matrices with the diagonal terms of modal mass $m_1^*, \ldots, m_n^*$, modal stiffness $k_1^*, \ldots, k_n^*$, and modal damping $c_1^*, \ldots, c_n^*$, respectively.

Eq. (2) is equivalent to n single-degree-of-freedom systems as follows ($i = 1, \ldots, n$),

$$\ddot{q}_i(t) + \omega_i^2 q_i(t) + 2\omega_i\xi_i\dot{q}_i(t) = \frac{p_i(t)}{m_i^*} \tag{4}$$

where $q_i(t)$ and $p_i(t)$ are the i-th components of $\boldsymbol{q}(t)$ and $\boldsymbol{p}(t)$, respectively, ω_i and ξ_i are the undamped natural frequency and damping ratio of the i-th mode, respectively.

As introduced in Section 1, existing wheel-rail force estimation methods usually assume that vehicle parameters $\mathbf{M}$, $\mathbf{K}$, and $\mathbf{C}$ are

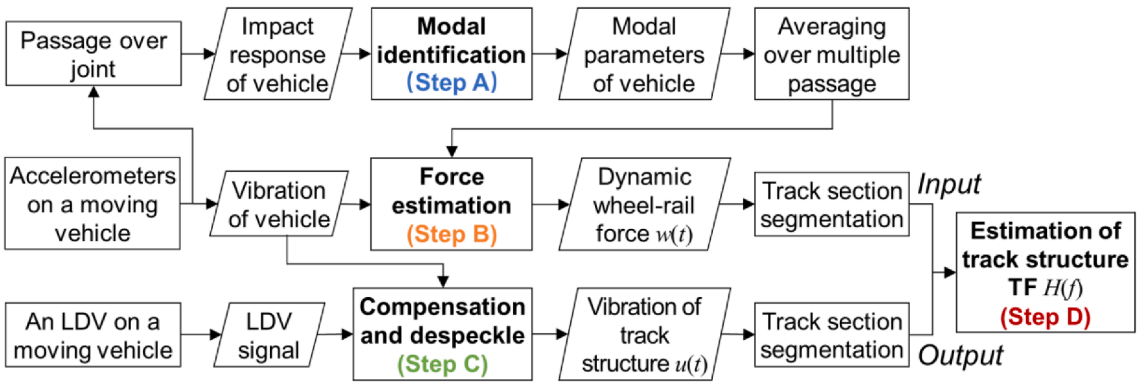

Fig. 1. Flowchart of the proposed methodology.

known, but this requirement is often difficult or expensive to fulfill. Therefore, we identify modal parameters (natural frequencies, damping ratios, mode shape vectors, and modal masses) of the vehicle under operational conditions so as to eliminate the need to define the vehicle parameters.

2.1.1. Operational modal identification

Insulated joints are widely present in railway tracks to provide electrical isolation between two rail circuits [8], and the passage of a wheel over a joint induces a significant impact force on the vehicle. Such impact can excite the vehicle modes over a wide range of frequencies, so the impact response measured by the accelerometers carries the dynamic characteristics of the vehicle. Other types of rail local irregularities can be used as alternative sources, such as degraded welds, switches and crossings, and rail surface defects. We employ the enhanced frequency domain decomposition [27,28] to extract these characteristics, and the main steps are given as follows.

A.1 Estimate the power spectrum density (PSD) matrix of measured impact response using Welch's averaged periodogram method [29]. Considering the decay pattern of impact response, using an exponential window in this procedure is recommended.

A.2 Apply singular value decomposition to the PSD matrix at each discrete frequency f to obtain a diagonal matrix containing singular values and a unitary matrix containing singular vectors corresponding to the singular values [27].

A.3 Plot the spectrum of leading singular values and pick up resonance peaks in the frequency range of interest, which indicate the possible existence of vehicle modes. Multiple levels of leading singular values can be used in cases of closely spaced modes [27].

A.4 For each resonance peak, compare the singular vectors of adjacent frequencies, for example, using the modal assurance criterion [30]. If they are of high similarity, a vehicle mode can be confirmed.

A.5 For the i-th vehicle mode, create an auto PSD using only the singular values of frequencies near the peak and apply inverse Fourier transform to the auto PSD to obtain an autocorrelation function. Then, estimate the damped natural frequency $\omega_{\mathrm{d}i}$ and the logarithmic decrement δ_i using the zero crossings and extremes of the autocorrelation function, respectively [28]. Further, calculate the undamped natural frequency ω_i and the damping ratio ξ_i as follows [28].

$$\xi_i = \frac{\delta_i}{\sqrt{\delta_i^2 + 4\pi^2}} \tag{5}$$

$$\omega_i = \frac{\omega_{\mathrm{d}i}}{\sqrt{1 - \xi_i^2}} \tag{6}$$

A.6 For the i-th vehicle mode, normalize each singular vector at frequencies near the peak and rotate each complex component to 0° (or 180°) if its phase lies in the first or fourth (or the second or third) quadrant [30]. Average all these real-valued vectors to obtain the mode shape vector of the i-th vehicle mode, denoted as φ_i.

A.7 Construct the mode shape matrix $\mathbf{\Phi}$ with all φ_i. Construct the mass matrix $\mathbf{M}$ with at least one known mass, such as the mass of an axle box. Determine the unknown masses by making $\mathbf{\Phi}^{\mathrm{T}}\mathbf{M}\mathbf{\Phi}$ a diagonal matrix, thus ensuring the diagonal property of $\mathbf{M}^*$. Calculate the modal mass matrix $\mathbf{M}^*$ that contains all m_i^* by $\mathbf{M}^* = \mathbf{\Phi}^{\mathrm{T}}\mathbf{M}\mathbf{\Phi}$.

The above method can produce the natural frequencies ω_i and $\omega_{\mathrm{d}i}$, damping ratio ξ_i, mode shape vector φ_i, and modal mass m_i^* of the n vehicle modes ($i = 1, \ldots, n$). This eliminates the need to pre-define the vehicle stiffness, vehicle damping, and part of the vehicle masses (e.g., the vehicle body mass) for wheel-rail force estimation. The modal identification results can be averaged over multiple passages of different joints, and the vehicle modal parameters can then be updated regularly and used for estimating the wheel-rail force $\boldsymbol{w}(t)$ from measured vehicle vibrations $\ddot{\boldsymbol{x}}(t)$. This helps reduce force estimation errors due to variations and uncertainties in the vehicle parameters.

2.1.2. Time-domain force estimation

Based on the vehicle modal parameters identified in Section 2.1.1, the wheel-rail force on the vehicle $\boldsymbol{w}(t)$ can be estimated from measured vehicle vibrations $\ddot{\boldsymbol{x}}(t)$ through the following steps. This method is adapted from the time-domain method proposed in [17]. Since wheel-rail contact forces are applied on wheels, only the elements in $\boldsymbol{w}(t)$ corresponding to forces on wheels are estimated, and the rest are constrained to zero in the estimation process. The derivation of the following equations can be found in the Appendix.

B.1 At the s-th time step, convert the measured acceleration $\ddot{\boldsymbol{x}}(t_s)$ to modal acceleration $\ddot{\boldsymbol{q}}(t_s)$ according to Eq. (3). For the i-th mode, estimate the i-th element of the modal force vector $\boldsymbol{p}_{\mathrm{d}}(t_{s\text{-}1})$ as follows using the current modal acceleration $\ddot{q}_i(t_s)$ and the previous modal displacement and velocity $q_i(t_{s-1})$, $\dot{q}_i(t_{s-1})$ [17]. Use zero initial condition when $s = 1$, i.e.,$q_i(t_0) = 0$ and $\dot{q}_i(t_0) = 0$.

$$p_{\mathrm{d}i}(t_{s-1}) = \frac{m_i^* \sin(\omega_{\mathrm{d}i}\Delta t)\left(\left(2\omega_i^2\xi_i^2 - \omega_i^2\right)\dot{q}_i(t_{s-1}) + \omega_i^3\xi_i q_i(t_{s-1})\right)}{\omega_i\xi_i\sin(\omega_{\mathrm{d}i}\Delta t) - \omega_{\mathrm{d}i}\cos(\omega_{\mathrm{d}i}\Delta t)} + \frac{m_i^*\omega_{\mathrm{d}i}\cos(\omega_{\mathrm{d}i}\Delta t)\left(-\omega_i^2 q_i(t_{s-1}) - 2\omega_i\xi_i\dot{q}_i(t_{s-1})\right) - m_i^*\omega_{\mathrm{d}i}e^{\omega_i\xi_i\Delta t}\ddot{q}_i(t_s)}{\omega_i\xi_i\sin(\omega_{\mathrm{d}i}\Delta t) - \omega_{\mathrm{d}i}\cos(\omega_{\mathrm{d}i}\Delta t)} \tag{7}$$

B.2 Convert the calculated modal force vector $\boldsymbol{p}_{\mathrm{d}}(t_{s\text{-}1})$ to a force vector $\boldsymbol{w}_{\mathrm{d}}(t_{s\text{-}1})$ according to Eq. (3). Constrain the elements of $\boldsymbol{w}_{\mathrm{d}}(t_{s\text{-}1})$ without wheel-rail forces to zero, denoted as $\boldsymbol{w}(t_{s\text{-}1})$. Then, convert the corrected force $\boldsymbol{w}(t_{s\text{-}1})$ back to the modal force $\boldsymbol{p}(t_{s\text{-}1})$ according to Eq. (3).

B.3 Calculate the modal displacement and velocity at the current step $q_i(t_s)$, $\dot{q}_i(t_s)$ as follows, using the corrected modal force $p_i(t_{s\text{-}1})$

[17].

$$q_i(t_s) = e^{-\omega_i\xi_i\Delta t}\sin(\omega_{\mathrm{di}}\Delta t)\left(\frac{\dot{q}_i(t_{s-1}) + \omega_i\xi_i q_i(t_{s-1})}{\omega_{\mathrm{di}}} - \frac{\xi_i p_i(t_{s-1})}{m_i^*\omega_i\omega_{\mathrm{di}}}\right) + e^{-\omega_i\xi_i\Delta t}\cos(\omega_{\mathrm{di}}\Delta t)\left(q_i(t_{s-1}) - \frac{p_i(t_{s-1})}{m_i^*\omega_i^2}\right) + \frac{p_i(t_{s-1})}{m_i^*\omega_i^2} \tag{8}$$

$$\dot{q}_i(t_s) = e^{-\omega_i\xi_i\Delta t}\sin(\omega_{\mathrm{di}}\Delta t)\left(\frac{(1-\xi_i^2)p_i(t_{s-1})}{m_i^*\omega_{\mathrm{di}}} - \omega_{\mathrm{di}}q_i(t_{s-1})\right) + e^{-\omega_i\xi_i\Delta t}\cos(\omega_{\mathrm{di}}\Delta t)\left(\dot{q}_i(t_{s-1}) + \omega_i\xi_i q_i(t_{s-1}) - \frac{\xi_i p_i(t_{s-1})}{m_i^*\omega_i}\right) - \omega_i\xi_i q_i(t_s) + \frac{\xi_i p_i(t_{s-1})}{m_i^*\omega_i} \tag{9}$$

B.4 Increase s by a time step and repeat the above process till reaching the signal end.

B.5 Detrend the estimated force $\boldsymbol{w}(t)$ by filtering it with a high-pass filter.

2.2. Output: Despeckle and compensation

In the proposed methodology, the vibration response of track components is continuously measured by an LDV on the moving vehicle. Speckle noise is inevitable due to the significant in-plane motion of the laser spot on the track surface, and the characteristics of speckle noise vary with the vehicle speed [20]. In this paper, we reduce speckle noise in a raw LDV signal $u_{\mathrm{r}}(t)$ using a signal processing method that is capable of working effectively at different speeds [25]. Meanwhile, the vibrations of the LDV and other optical components along the laser beam affect the relative velocity between the laser head and the target. These vibrations are measured and denoted as $\dot{x}_{\mathrm{c}_1}(t), \dot{x}_{\mathrm{c}_2}(t), \ldots$, and their effect on the LDV signal is compensated for. The despeckle and compensation steps are given as follows.

C.1 Perform one-level Haar wavelet decomposition and reconstruction to $u_{\mathrm{r}}(t)$ and calculate spike indicators $r(t)$ as follows [20],

$$d(t) = \mathrm{DWT_D}[u_{\mathrm{r}}(t)] \tag{10}$$

$$r(t) = |\mathrm{IDWT_D}[d(t)]| \tag{11}$$

where $\mathrm{DWT_D}[\cdot]$ and $\mathrm{IDWT_D}[\cdot]$ represent forward and inverse discrete wavelet transforms, respectively, and $d(t)$ denotes the detail coefficients. Label P% locations in $u_{\mathrm{r}}(t)$ with the largest spike indicators $r(t)$ as spikes.

C.2 Define an autoregressive integrated moving average (ARIMA) model with an autoregressive order p_{A}, a moving average order q_{A}, and a differencing order d_{A}. Train the ARIMA model with $u_{\mathrm{r}}(t)$ along the forward direction and replace the labeled points sequentially with predictions from the ARIMA model [20]. This process is called imputation in [20]. Repeat the above training and replacement process along the backward direction, and then average the forward and backward replacements as the reconstructed signal $u_{\mathrm{p}}(t)$.

C.3 Subtract $\dot{x}_{\mathrm{c}_1}(t), \dot{x}_{\mathrm{c}_2}(t), \ldots$ from the reconstructed signal $u_{\mathrm{p}}(t)$ as follows.

$$u_{\mathrm{t}}(t) = u_{\mathrm{p}}(t) - \sum_j \dot{x}_{\mathrm{c}_j}(t) \tag{12}$$

C.4 Apply a band-pass filter with the cut-off frequency of f_{L} and f_{H} to $u_{\mathrm{t}}(t)$, resulting in the extracted structural vibration $u(t)$.

The effectiveness of the above method requires a proper selection of its parameters. Based on the previous research [20,25], we recommend using $d_{\mathrm{A}} = 1$, $q_{\mathrm{A}} = 1$ and setting f_{L} and f_{H} to the lowest and highest frequencies of interest for track vibrations, respectively. The parameters P% and p_{A} should be tuned considering the despeckle performance and the computational cost at different speeds, which can be achieved either quantitatively based on simulated signals or qualitatively through trial and observation based on measured signals [25]. Once these parameters are defined, the method can be applied to LDV measurements without adjusting its parameters for different vehicle speeds.

2.3. Transfer function estimation

A railway track is a continuous structure. When measuring its TFs from a running vehicle, the load and response locations move, and the input–output relationship varies. Considering the variation in track dynamic properties between different locations, we divide track structures into distributed sections and estimate a TF using measurements on each track section, representing the average input–output relationship for the track section. Each track section should not be too long; otherwise, we cannot capture the variation within it. It should also not be too short; otherwise, insufficient data points can cause large errors and poor frequency resolution. Once the track section length is defined, the estimated wheel-rail force $w(t)$ and the measured track vibration $u(t)$ can be cut for each track section, which can be used as the input and output for TF estimation, respectively.

Non-parametric methods for estimating a TF from the input and output signals of a system have been studied for decades [31–34]. Essentially, they smooth the ratio of the output spectrum to the input spectrum using different strategies, such as windowing and averaging, for the purpose of reducing errors caused by noise, transient, and leakage [32–34]. In this paper, assuming that the noise is uncorrelated with the excitation, we use the so-called $\mathrm{H_1}$ estimator to calculate the TF of a track section. The main steps are given as follows.

D.1 For each track section, divide $w(t)$ and $u(t)$ into overlapping segments and taper each segment with a window function.

D.2 Estimate the cross PSD of $w(t)$ and $u(t)$, denoted as $P_{uw}(f)$, and the auto PSD of $w(t)$, denoted as $P_{ww}(f)$, again using Welch's averaged periodogram method [29].

D.3 Calculate the TF in terms of a receptance function with the input of the wheel-rail force and the output of the track displacement, as follows [31,32].

$$H(f) = \frac{P_{uw}(f)}{2\pi f \cdot P_{ww}(f)} \tag{13}$$

Fig. 2 presents the flowchart of all the steps described above for estimating track structure TFs, which essentially details Steps A–D in Fig. 1. The proposed methodology will be tested and validated in the next section.

3. Laboratory Validation

3.1. Experimental setup

We validate the proposed methodology in a vehicle-track test rig of TU Delft named V-Track [35], as shown in Fig. 3. The scaled track structure consists of rails, sleepers, and track slabs. The rails are supported by the sleepers through fasteners and rail pads, and the sleepers are assembled on the track slabs through bolts and sleeper pads. Joints are used to connect different rail pieces. The vehicle system consists of a vehicle body suspended on an axle box with a wheel. The suspension provides not only stiffness and damping but also a static wheel load. There are two such vehicle systems (Vehicle A and Vehicle B) assembled symmetrically at the ends of a rotating beam. As the beam rotates, the vehicles move forward, and the wheels roll along the rails. In our measurements, the wheels are cylindrical to replicate tread-rail head contact, and the angle of attack of the wheels with respect to the rails is zero so that the wheels run along the tangent of the track. Additionally, the vehicles cannot move laterally or tilt due to the constraint of the beam. Therefore, we validate the proposed methodology under conditions more similar to straight tracks.

As shown in Fig. 3(a), we instrument the moving platform of V-Track with an LDV and accelerometers. A Polytec RSV-150 LDV is mounted on the center of the beam, and a mirror is fixed at the end of the beam to direct the laser downward onto the track with a fixed offset from the wheel. As the vehicle moves, the laser spot scans along the track and measures the vertical track vibration excited by the moving vehicle. As mentioned in Section 2.2, the vibrations of the LDV and other optical components can affect the LDV signal. Since the LDV is mounted horizontally on the center of the beam, it has little vibration along the laser beam direction and, thereby, little effect on the LDV signal. In contrast, the mirror mounted on the vehicle vibrates significantly, so an accelerometer is mounted on the mirror to compensate for its effect on the LDV signal. This setup resembles both the scanning and vibration of an LDV installed on a train. Meanwhile, four PCB 356B21 accelerometers are mounted on the upper and the lower masses of the vehicle to estimate the dynamic wheel-rail forces. Additionally, the angular position of the rotating beam is measured to determine the position of the wheels. As shown in Fig. 3(b), we instrument some track sections with accelerometers to measure their vertical vibrations for comparisons.

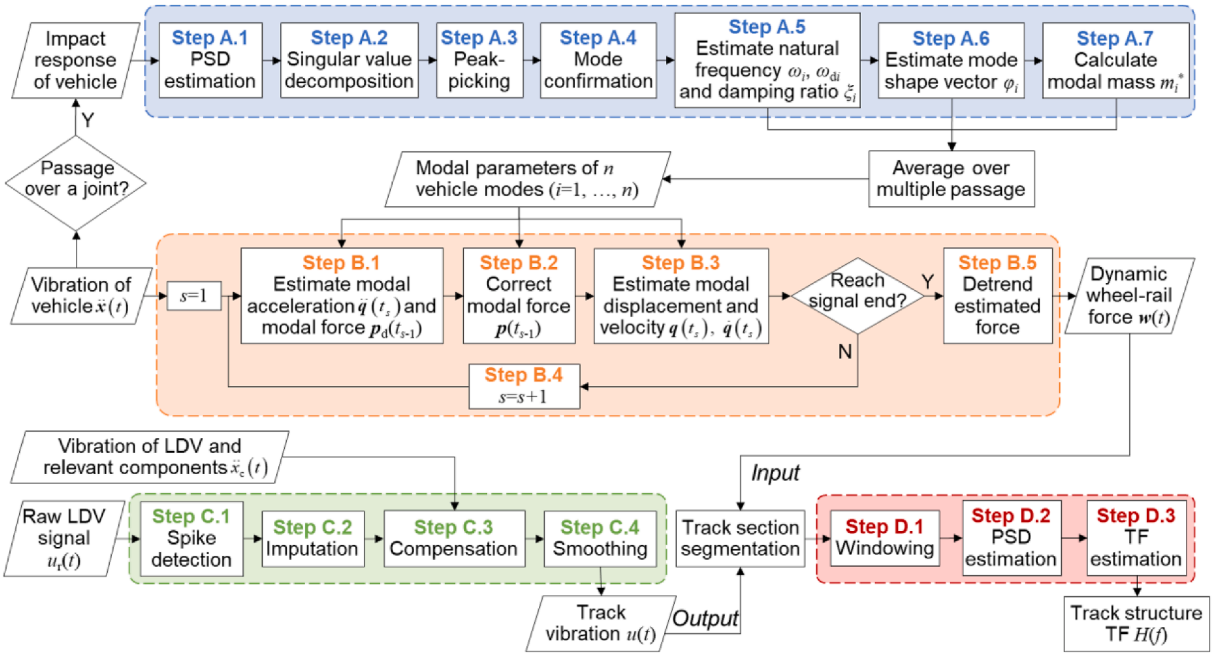

Fig. 2. Flowchart of the proposed steps.

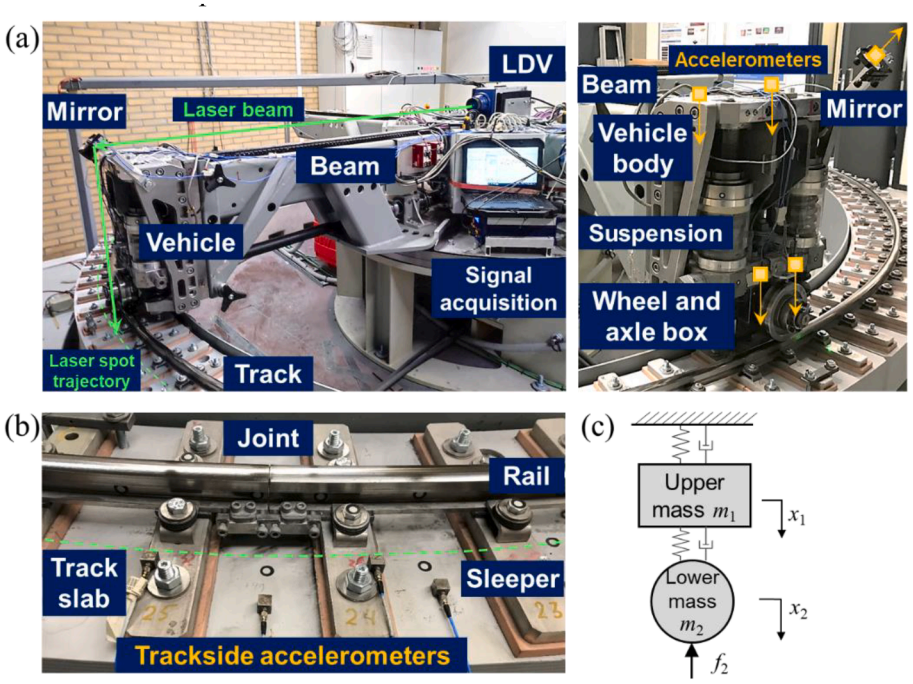

Fig. 3. Experiment setup and vehicle model. (a) V-Track test rig and the instrumentation; (b) Trackside sensors; (c) Model of the vehicle system.

3.2. *Modal identification and force estimation*

We use the model in Fig. 3(c) to represent the vertical dynamics of the vehicle in V-Track. Each of the two masses has one degree of freedom of bouncing. The spring and damper between them represent the suspension, and those on top represent the combined stiffness and damping from both the connection of the vehicle body on the rotating beam and the flexibility of the rotating beam. A force is applied on the lower mass, representing the contact force on the wheel. For Vehicles A and B, the lower mass represents the wheel and axle box with their total mass known ($m_2 = 40$ kg), while the upper mass represents the combination of the vehicle body mass and part of the rotating beam mass, so the total mass m_1 is unknown. All the stiffness and damping are also unknown.

3.2.1. *Modal identification*

According to Section 2.1.1, we use the impact response of each vehicle to identify its modal parameters. Fig. 4(a) and 4(b) show the vibrations of Vehicles A and B when passing over a joint at 4 km/h, respectively. The impact response caused by the passage of the joint

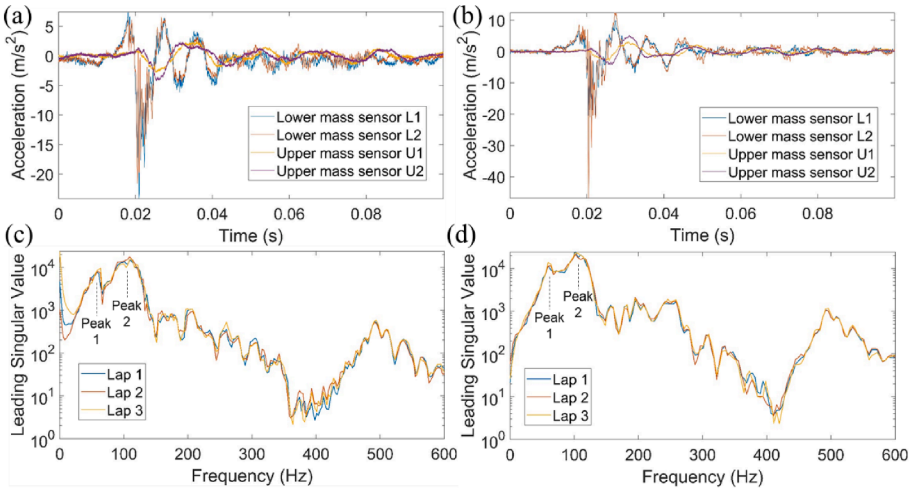

Fig. 4. Vehicle vibrations and singular value spectra. (a) Impact response of Vehicle A; (b) Impact response of Vehicle B; (c) Spectra of Vehicle A; (d) Spectra of Vehicle B.

can be clearly observed. Both masses show attenuated bouncing motions at relatively low frequencies, while the response of the lower mass contains more high-frequency components.

In order to reduce the effect of pitching motion and noise, we average the signals of the two sensors on each mass. Then, for each vehicle, we apply Steps A.1–A.3 to the averaged signals, and a singular value spectrum can be obtained for each passage over a joint. Fig. 4(c) and 4(d) plot such spectra calculated from different laps of measurements (at the same speed) for the two vehicles. The results show high repeatability between the different laps and also similarity between the two vehicles. For each vehicle, two dominant peaks below 150 Hz are confirmed through Step A.4.

The modal parameters corresponding to these two peaks are further identified through Steps A.5–A.7. After averaging over different speeds (2 km/h, 4 km/h, 6 km/h, 8 km/h), different joints, and different laps, we obtain the result in Table 1. It shows that the two peaks correspond to the in-phase and anti-phase bouncing motions of the two masses, respectively. Despite the identical design, the identified modal parameters of the two vehicles deviate slightly, highlighting the value of modal identification under operational conditions.

3.2.2. Force estimation

Before applying the time-domain force estimation method to estimate the wheel-rail force from measured vehicle vibrations, we first conduct a simulation case study to validate the force estimation method. Based on the vehicle model in Fig. 3(c), an artificial load is applied to the lower mass, and the accelerations of the two masses are obtained by solving the equations of motion of the model. The simulated accelerations are then superposed with randomly generated Gaussian noise to resemble the disturbance of measurement noise. The contaminated accelerations are shown in Fig. 5(a), and they are used to estimate the force on the lower mass through Steps B.1–B.5. The result is further compared with the applied force in Fig. 5(b). It can be observed that the force estimation method accurately estimates the applied force in both the transient phase and the stationary phase.

According to Section 2.1.2, the identified modal parameters in Table 1 are further used to estimate dynamic wheel-rail force through Steps B.1–B.5. Fig. 6(a) and 6(b) show the estimated forces using the accelerations of Vehicle A over a joint at different speeds. The results contain both positive and negative forces since static wheel loads are not included. Some residual drifts can also be observed but have little effect on the dynamic components and the TF estimation. High-frequency P1 force and low-frequency P2 force can be observed, and their amplitudes become larger as the vehicle speed increases.

Fig. 6(c) and 6(d) plot the estimated wheel-rail forces of Vehicle A using measurements on a normal track section. The low-frequency components are considered to be related to the vertical alignment of the track, while the high-frequency components are considered to be related to the local roughness of the wheel and rail. Meanwhile, the amplitude of the dynamic wheel-rail force becomes larger when the vehicle speed is higher.

3.3. Despeckle and compensation

In this section, we validate the despeckle and compensation method in Section 2.2. We divide the track structure of V-Track into overlapping track sections centered at each sleeper, and each track section has a length of around two sleeper spacings. Such segmentation enables the track structure to be characterized as a distributed system so that the estimated TF describes the track dynamic properties near each sleeper. Fig. 7 shows the measurement configurations of Vehicle A on two typical track sections. Considering the laser-wheel offset Δx, the wheel passes over the joint when the LDV measures Track section ①, while the wheel runs on a normal track section when the LDV measures Track section ④. For comparison, we mount three accelerometers (J1–J3 and T2–T4) on each track section.

First, measurements on Track section ① at different speeds are studied. We use $P\% = 30\%$, $p_A = 30$, $f_L = 50$ Hz, and $f_H = 1000$ Hz in Steps C.1–C.4. The despeckle and compensation results are shown in Fig. 8. The upper two plots compare the raw LDV signal, the reconstructed signal (after Step C.2), and the mirror vibration (after integration from acceleration to velocity). It shows that spikes are detected and replaced with reasonable predictions. The mirror vibration is dominant at low frequencies, so its effect must be compensated for. The lower two plots compare the LDV signal after despeckle and compensation (Steps C.1–C.4) with those measured by the trackside sensors (after integration from acceleration to velocity), which shows good agreement in the impact response phase as well as before and after the impact.

Fig. 9 presents the despeckle and compensation results for measurements on Track section ④. Although their amplitudes are generally lower than those on Track section ①, the proposed method is still effective in reducing speckle noise and providing results

Table 1
Identified modal parameters of the two vehicles.

Modes	Averaged modal parameters	Vehicle A	Vehicle B
Peak 1 (in-phase bounce)	Undamped natural frequency f_1	62.0 Hz	62.6 Hz
	Damping ratio ξ_1	0.15	0.11
	Normalized mode shape vector φ_1	$[0.83\ 1]^T$	$[0.74\ 1]^T$
	Modal mass m_1*	170.9	187.8
Peak 2 (anti-phase bounce)	Undamped natural frequency f_2	98.5 Hz	111.7 Hz
	Damping ratio ξ_2	0.09	0.14
	Normalized mode shape vector φ_2	$[-0.25\ 1]^T$	$[-0.2\ 1]^T$
	Modal mass m_2*	52.5	50.8

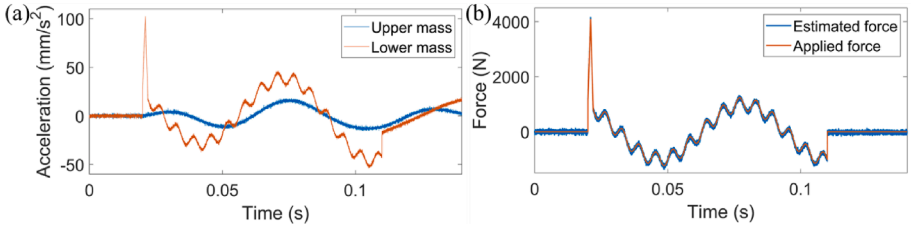

Fig. 5. Validation of the force estimation method with a simulation case. (a) Simulated vehicle vibrations; (b) Comparison between the estimated force and the applied force.

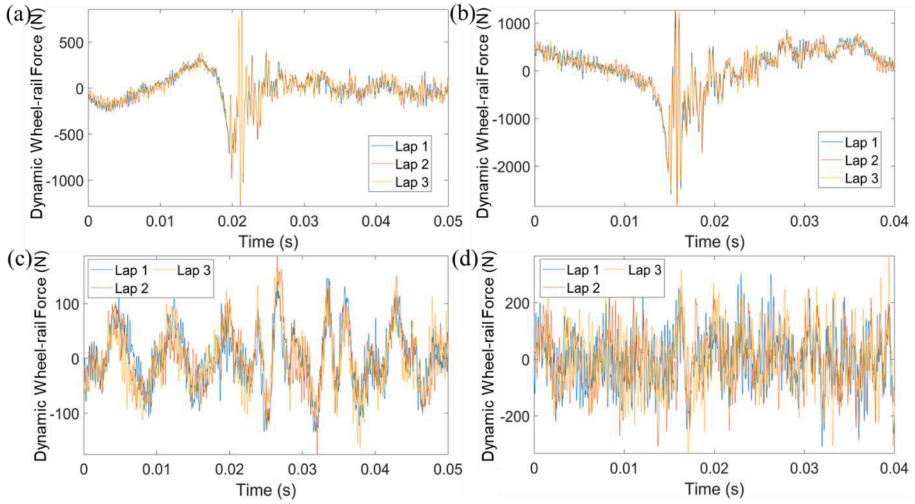

Fig. 6. Estimated dynamic wheel-rail forces of Vehicle A. (a) Passing over a joint at 8 km/h; (b) Passing over a joint at 16 km/h; (c) Running on a normal track section at 8 km/h; (d) Running on a normal track section at 16 km/h.

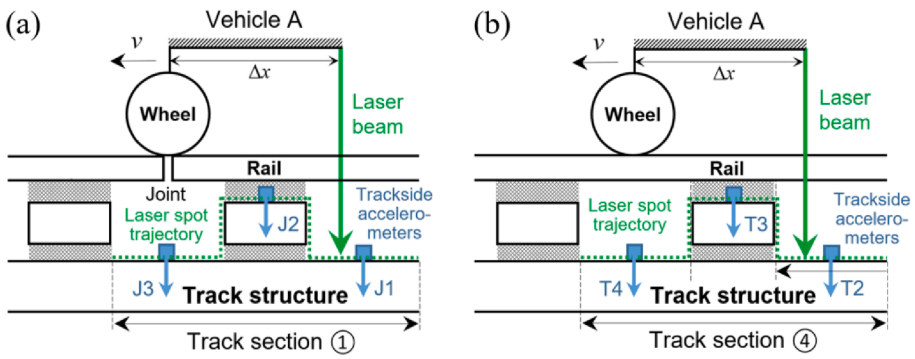

Fig. 7. LDV and trackside measurement on two track sections. (a) Track section ① with a joint; (b) Track section ④ without joints.

consistent with the trackside measurements. The above results demonstrate the effectiveness of the despeckle and compensation method at different speeds. Slight deviations between the LDV and trackside signals can be observed, caused by imperfect despeckle or compensation and spatial deviations between the laser spot and the accelerometers.

Additionally, it can be seen from Figs. 8 and 9 that the vibrations of the sleeper (J2 or T3) and the track slab (J1, J3 or T2, T4) are very close in the frequency range we are concerned with, as a consequence of the high sleeper pad stiffness in V-Track. This reflects the rationale for combining measurements on the sleeper and track slab (within one track section) for TF estimation, which provides more data points than using only measurement on a scaled sleeper.

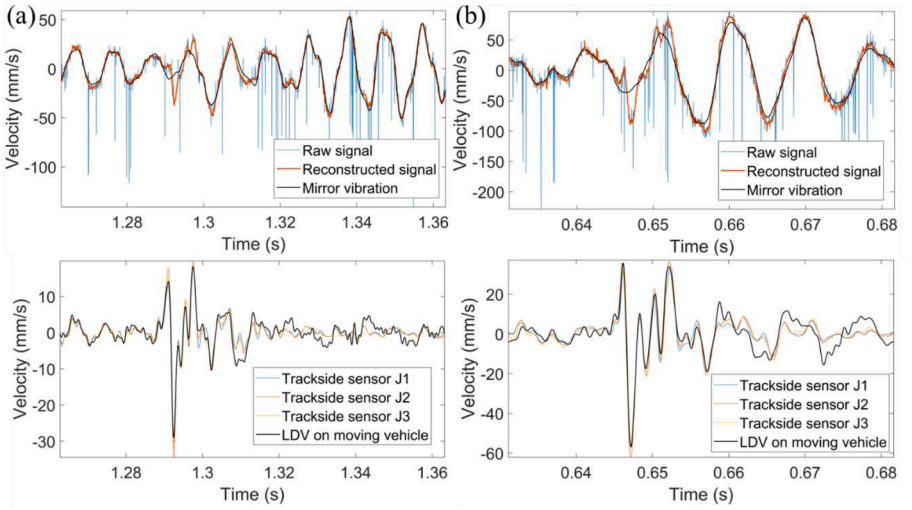

Fig. 8. Despeckle, compensation, and comparison with trackside measurements on Track section ①. (a) 8 km/h; (b) 16 km/h.

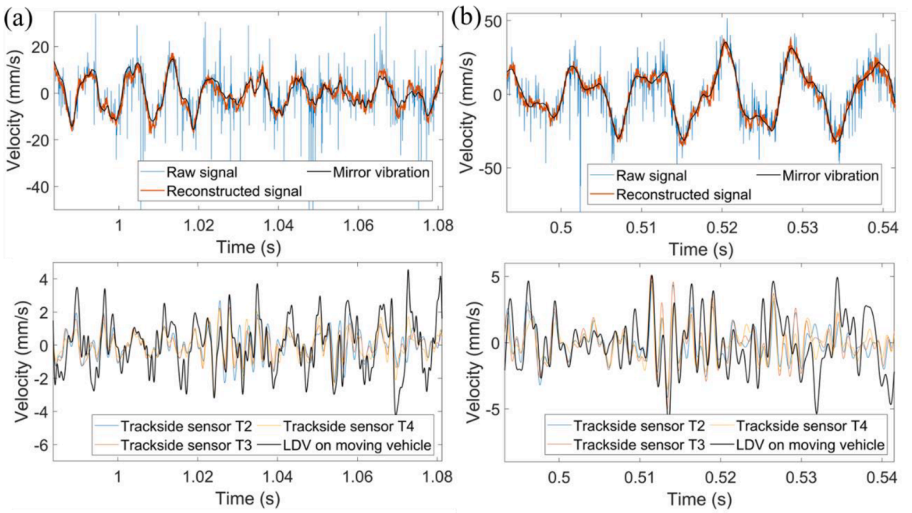

Fig. 9. Despeckle, compensation, and comparison with trackside measurements on Track section ④. (a) 8 km/h; (b) 16 km/h.

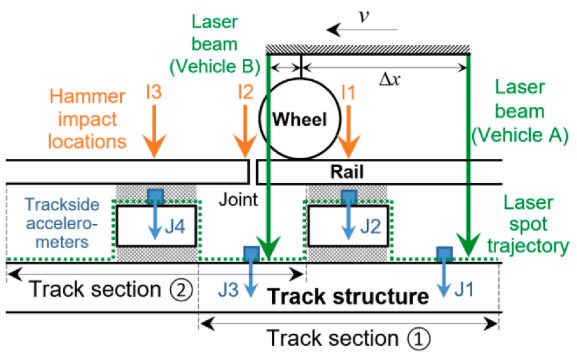

Fig. 10. Measurement and hammer tests on track sections with a joint.

3.4. Transfer function estimation and comparison

Based on the measured track vibration and the estimated wheel-rail force on each track section, a TF of the track structure can be estimated according to Section 2.3. We take several track sections as examples to showcase the estimation performance. In Step D.1, each signal is divided into three overlapping segments of 90 % of the section length. In Step D.2, a Hanning window is used. The estimated TFs hold the physical meaning (receptance) that is consistent with the conventional definition of track structure TFs or FRFs. This allows the TF measurement system on the moving vehicle to be validated using conventional trackside technology. Therefore, we perform hammer tests on these track sections using a PCB 086C03 hammer and the trackside accelerometers to obtain their FRFs. It is worth noting that we focus mainly on the shapes and resonance frequencies of the estimated TFs and the measured FRFs in this paper, rather than the absolute amplitude or phase characteristics.

3.4.1. Track sections with a joint

Fig. 10 shows the measurement configuration on Track sections ① and ②. Since Vehicles A and B have different laser-wheel offsets, they measure different track sections when passing over the joint. For Vehicle A (or Vehicle B), the laser spot is behind (or ahead of) the wheel and thereby measures Track section ① (or ②) when the wheel passes over the joint. Additionally, hammer tests are performed, with the impact locations denoted as I1–I3 and the trackside sensors denoted as J1–J4.

Fig. 11 (or Fig. 12) shows the TFs of Track section ① (or ②) estimated from the measurements on Vehicle A (or B) at two different speeds, in which the solid black line and the shaded area represent the mean and stand deviation of the estimates from different laps, respectively. We focus on the frequency range of 200–800 Hz as it belongs to the rigid-body motions (bouncing and rolling) of the sleepers under the wheel passage in V-Track [5], which are more related to the properties of the track structure, such as the support stiffness. Meanwhile, the small hammer used in the hammer tests can effectively excite the track modes in this frequency range. It can be seen that the frequency resolution decreases at a higher speed due to the shorter signal length. At frequencies below 600 Hz, the standard deviation is small, indicating good repeatability at different laps, while at higher frequencies, the standard deviation becomes larger. The frequency range of small standard deviations is broader at the higher speed, mainly because the vehicle moving at a higher speed generates larger excitations at higher frequencies.

The colored solid lines in Fig. 11(a) and 11(b) represent the average TFs estimated using signals from the trackside sensors instead of the LDV signal. The results of using the LDV and the trackside sensors are close to each other since the LDV signals after despeckle and compensation are very close to the trackside signals. This further demonstrates the accuracy of the track vibration measurement using the LDV on the moving vehicle.

Further, we compare the estimated TFs with FRFs from the hammer tests, where the impact and sensor locations correspond to the wheel-laser offset. A good agreement in their shapes and resonance frequencies can be observed, especially below 500 Hz, demonstrating the effectiveness of TF estimation on different vehicles and at different speeds. The two resonance peaks at 300–400 Hz in the FRFs are effectively captured by the estimated TFs from the moving vehicle. At frequencies above 500 Hz, the FRFs deviate from each other, representing different dynamic properties for different impact and sensor locations. Consequently, the estimated TFs show large standard deviations as the positions of the wheel and laser spot are moving, and the resonance frequencies of the estimated TFs deviate more from those of the FRFs. Additionally, the FRFs are smoother than the estimated TFs due to less noise and higher frequency resolution.

3.4.2. Track sections without joints

Similar measurements and comparisons are performed on three track sections without joints, as illustrated in Fig. 13. The TF estimates of Vehicles A and B on Track section ③ are shown in Figs. 14 and 15, respectively. By comparing them with the FRFs from the

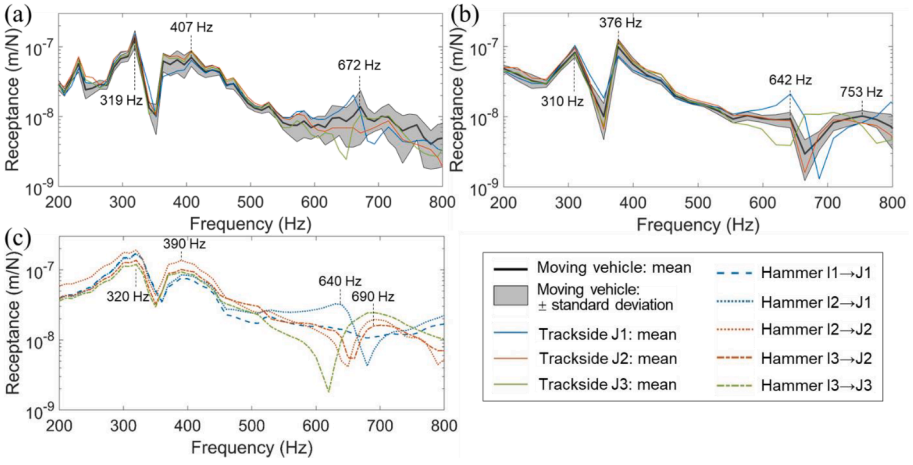

Fig. 11. TF estimation and comparison on Track section ① (Vehicle A). (a) 8 km/h; (b) 16 km/h; (c) Hammer tests.

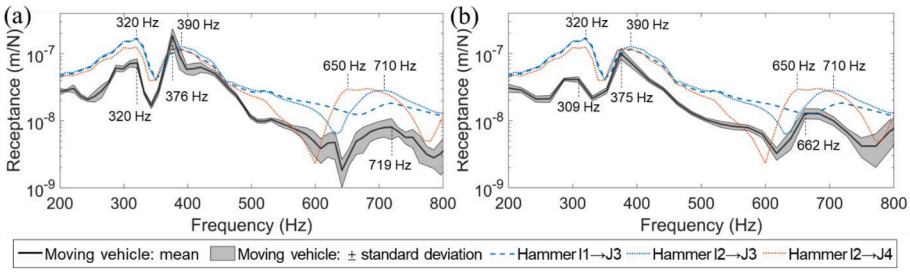

Fig. 12. TF estimation and comparison on Track section ② (Vehicle B). (a) 8 km/h; (b) 16 km/h.

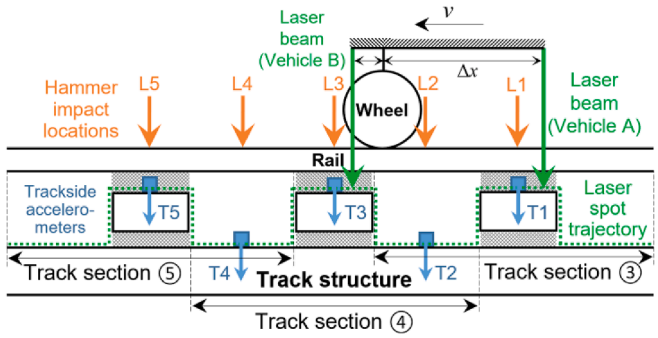

Fig. 13. Measurement and hammer tests on track sections without joints.

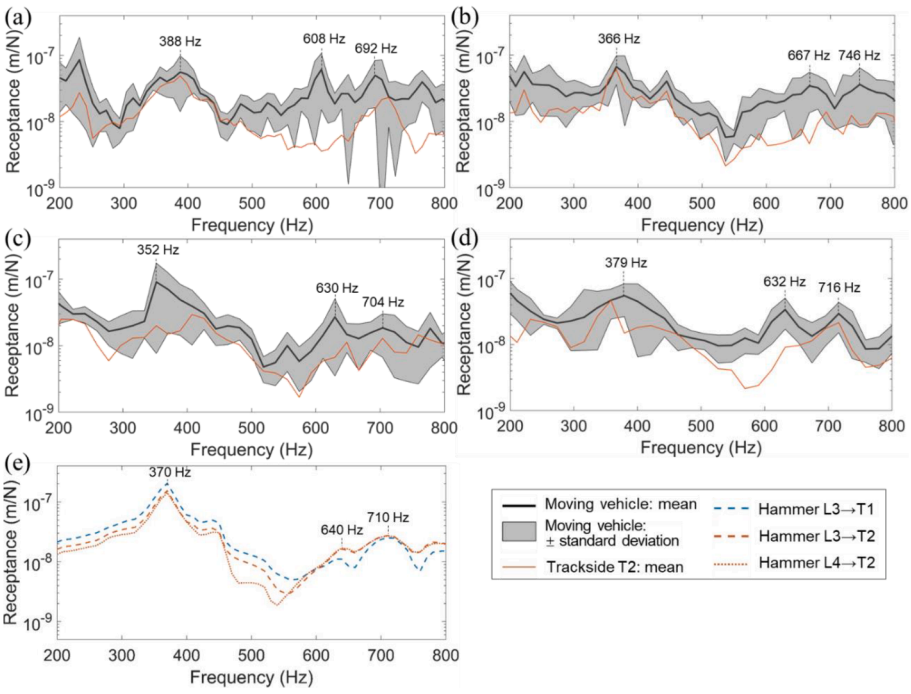

Fig. 14. TF estimation and comparison on Track section ③ (Vehicle A). (a) 8 km/h; (b) 10 km/h; (c) 14 km/h; (d) 16 km/h; (e) Hammer tests.

hammer tests, we can see good agreement in their shapes and resonance frequencies at different speeds. As the vehicle speed increases, their deviation increases at low frequencies and decreases at high frequencies, which is consistent with the simulation result in [26]. Additionally, the differences between the TF estimates on Vehicles A and B are caused by the different positions of the wheels when measuring this track section.

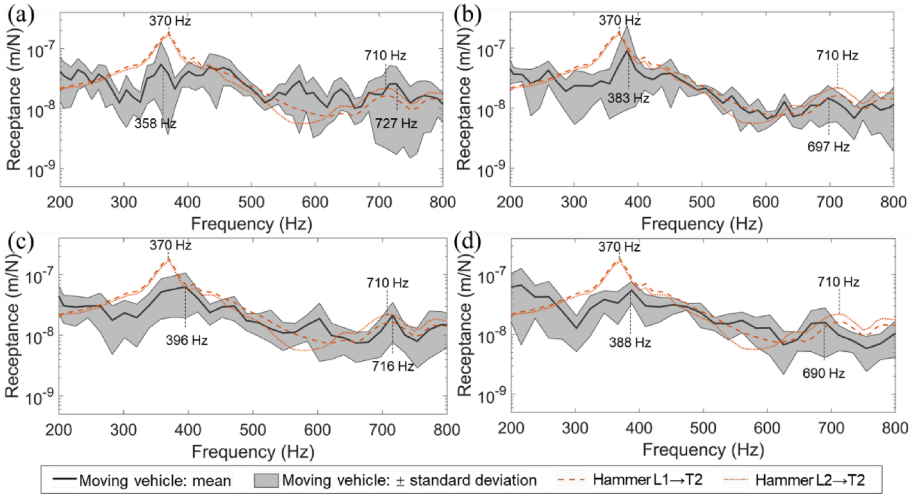

Fig. 15. TF estimation and comparison on Track section ③ (Vehicle B). (a) 8 km/h; (b) 10 km/h; (c) 14 km/h; (d) 16 km/h.

By comparing Figs. 14 and 15 with Figs. 11 and 12, we can see that there is one dominant peak in the frequency range of 300–400 Hz on the track section without joints whereas there are two on the track sections with a joint. This difference reflects the variation in track dynamic properties between these sections. Additionally, the standard deviations of the estimates on the track sections with the joint are generally smaller than those without joints. This confirms that excitations with large amplitude and broad frequency bands improve the TF estimation performance.

The TF estimation results on Track sections ④ and ⑤ are shown in Figs. 16 and 17, respectively. The estimated TFs are in good agreement with the measured FRFs and capture the dominant resonance peaks. As the vehicle speed increases, their deviation at high frequencies becomes smaller, whereas that at low frequencies becomes larger. The results demonstrate the effectiveness of TF estimation on normal track structures at different speeds.

In this paper, we focus on the shapes and the resonance frequencies of the TFs and FRFs since they depend strongly on the track dynamic properties, such as the track stiffness, thus being useful for structural health monitoring. Nevertheless, deviations in both frequency and amplitude can be observed, and the possible reasons are discussed as follows.

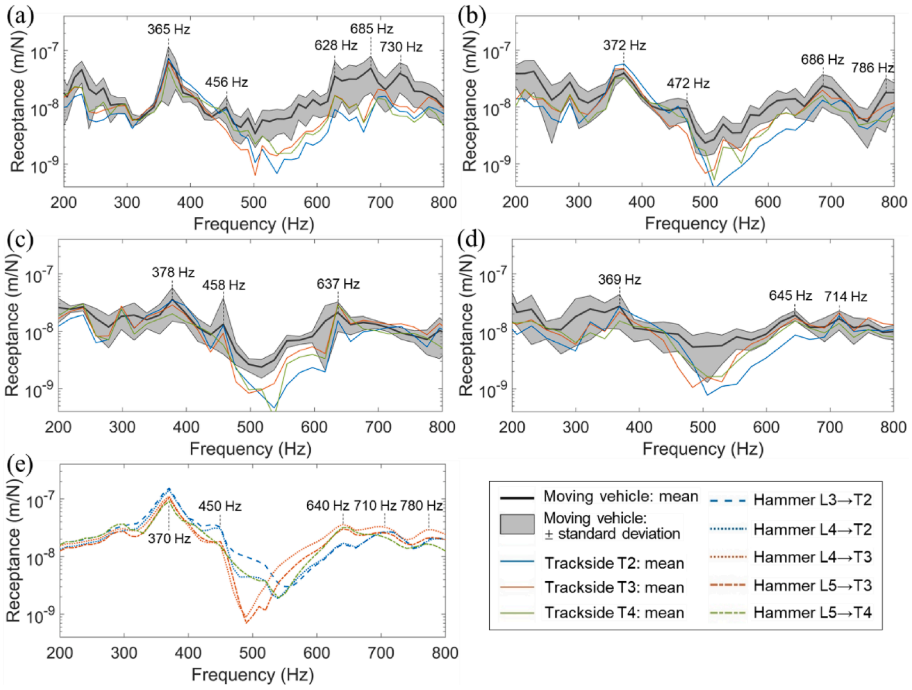

Fig. 16. TF estimation and comparison on Track section ④ (Vehicle A). (a) 8 km/h; (b) 10 km/h; (c) 14 km/h; (d) 16 km/h; (e) Hammer tests.

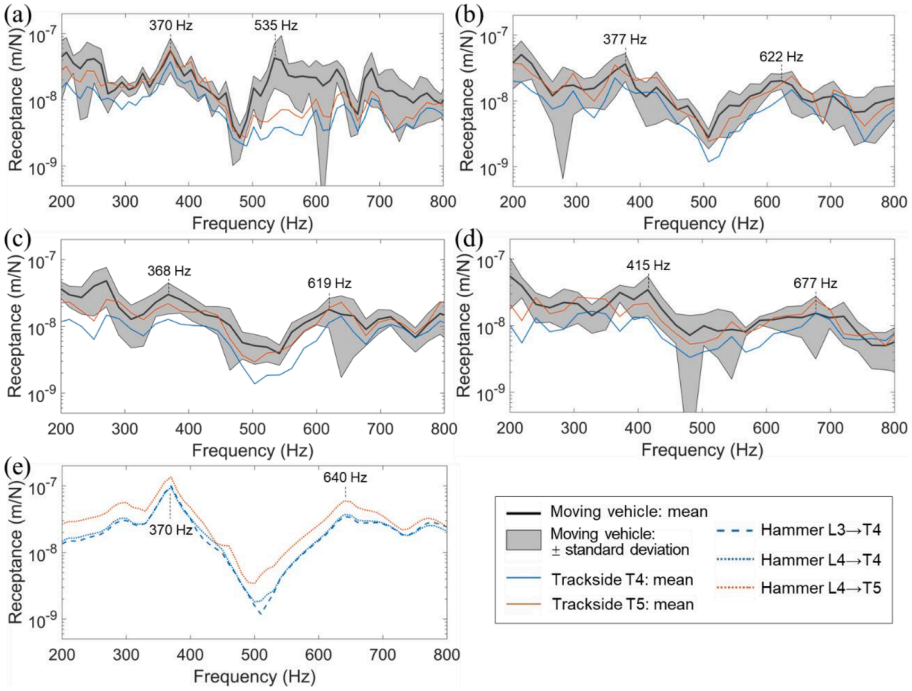

Fig. 17. TF estimation and comparison on Track section ⑤ (Vehicle B). (a) 8 km/h; (b) 10 km/h; (c) 14 km/h; (d) 16 km/h; (e) Hammer tests.

- The track properties, such as stiffness and damping, can differ from unloaded conditions to loaded conditions due to the nonlinearity of track components. The developed system on the moving vehicle has the advantage of measuring the TFs under loaded conditions, whereas the hammer tests measure the FRFs without vehicle loads.
- Errors in the vehicle model for wheel-rail force estimation are considered to be the main source of errors in the TF estimation since the accuracy of the track response measurement and the force estimation method has been verified. Errors in the vehicle parameters can be reduced by regularly updating the vehicle model through the operational modal identification.
- Vehicles A and B are assembled symmetrically on the rotating beam, which affects each other primarily through the rotating beam and secondarily through the track structure. This paper assumes a single input for each vehicle and a single input for the track structure, so each vehicle is an additional excitation source for the other vehicle and the track structure, thus affecting the force and

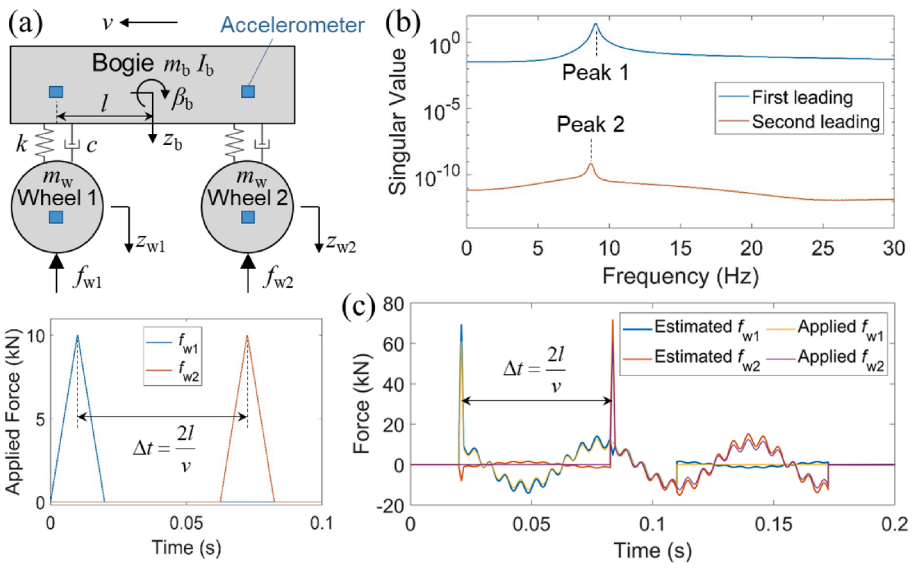

Fig. 18. Simulation study on a bogie. (a) Bogie model; (b) Singular value spectra; (c) Comparison between the estimated forces and the applied forces.

TF estimation. Our vibration measurements show that such influence is negligible, so decoupling the two vehicles in the TF estimation is still reasonable.

4. Discussions

This paper demonstrates the TF measurement system on a scaled test rig in our laboratory. While its application in real fields is beyond the scope of this paper, this section aims to discuss the potential applicability of the methodology when faced with challenges closer to real fields.

A simulation study of a bogie with two wheels is considered, as shown in Fig. 18(a). It has four degrees of freedom (z_b, β_b, z_{w1}, z_{w2}) and two input forces on the two wheels (f_{w1}, f_{w2}). The forces are assumed to be identical, but there is a time delay due to the distance between the two wheels. Four accelerometers are used to measure the vibration response. This bogie model is used to investigate the applicability of the modal identification and force estimation methods (in Section 2.1) to vehicles with multiple wheels and modes of similar frequencies.

This bogie has four modes – two rigid motions at 0 Hz (due to insufficient constraints) and the bouncing and pitching of the bogie relative to the wheels at two respective frequencies. To resemble the case of closely spaced modes, the mass and stiffness parameters of the bogie are adjusted to overlap the bouncing and pitching frequencies. Then, as shown in Fig. 18(a), impact forces are applied to the two wheels to simulate their passage over a joint, and the accelerations at the four sensor locations are obtained. According to Section 2.1.1, the first two levels of leading singular values are calculated and plotted in Fig. 18(b). Each level exhibits one resonance peak, and the modal parameters of the two peaks are identified and presented in Table 2. Meanwhile, the theoretical results of the bogie modes are derived through eigenvalue analysis and compared in Table 2. Despite the very close frequencies of the two modes, the method effectively identifies their modal parameters, demonstrating the applicability of the modal identification method to distinguish between closely spaced modes.

Further, forces similar to that in Fig. 5 are applied to the two wheels, and the accelerations at the sensor locations are computed using the bogie model. The simulated accelerations are superposed with Gaussian noise and then used to estimate the dynamic forces on the two wheels according to Section 2.1.2. The modal parameters identified above are used for the force estimation. The estimated forces are compared with the applied forces in Fig. 18(c), and their agreement demonstrates the applicability of the force estimation method to multiple wheels. The estimation error for one wheel becomes pronounced when the other wheel is subject to a large impact force, reflecting the mutual interference between the two wheels on the bogie. The estimated wheel-rail dynamic forces can be further combined with track vibrations measured by an LDV to estimate track structure TFs with multiple inputs.

5. Conclusions

This paper develops a novel track structure TF measurement system and the associated TF estimation methodology based on LDV and accelerometer on a moving vehicle. Enhanced frequency domain decomposition is applied to vehicle impact response over a joint to obtain its modal parameters, which further support the estimation of dynamic wheel-rail forces from vehicle vibrations using a Duhamel integral-based method. A despeckle and compensation method is applied to LDV signals to reduce speckle noise and extract track vibrations. A TF is then estimated for each track section using the estimated wheel-rail force as input and the measured track vibrations as output. This methodology is validated on different sections of a scaled vehicle-track test rig at different speeds through comparisons with trackside measurements and hammer tests. The main conclusions are summarized as follows.

(1) The modal identification method eliminates the need to pre-define the vehicle stiffness, vehicle damping, and vehicle body mass for wheel-rail force estimation and enables the vehicle modal parameters to be updated under operational conditions.
(2) The LDV and accelerometer measurements provide TF estimates that are in good agreement in terms of the shapes and resonance frequencies with the FRFs measured from hammer tests at 200–800 Hz. Such effectiveness holds for the whole vehicle speed range tested, from 8 km/h to 16 km/h.
(3) The standard deviation of the TF estimates becomes larger at high frequencies due to the variation of track dynamics when the wheel and laser spot are moving. Among the speeds tested, a higher vehicle speed yields smaller standard deviations of the estimated TFs over different laps and also smaller deviations between the estimated TFs and the measured FRFs at high frequencies.

Table 2
Comparison between the identified modal parameters and the theoretical results.

Modes	Averaged modal parameters	Identification	Theory (neglect damping)
Peak 1 (bogie pitching)	Undamped natural frequency	9.04 Hz	9.04 Hz
	Damping ratio	0.03	/
	Normalized mode shape vector	$[1\ -0.76\ -0.09\ 0.84]^T$	$[1\ -1\ 0\ 0.75]^T$
Peak 2 (bogie bouncing)	Undamped natural frequency	8.71 Hz	8.72 Hz
	Damping ratio	0.03	/
	Normalized mode shape vector	$[0.89\ 1\ -0.78\ -0.21]^T$	$[1\ 1\ -0.8\ 0]^T$

(4) Unlike conventional hammer tests that can only be applied at one location at a time, usually without vehicle loads, the proposed TF measurement system can continuously scan track structures and measure their TFs under loaded conditions.
(5) The differences in the shapes and resonance frequencies of the estimated TFs between different track sections reflect the variation of track dynamic properties, suggesting that the system has the potential to be used for structural health monitoring of railway tracks.

To further reduce errors in wheel-rail force estimation, the proposed method will be improved in the robustness to model errors. Different TF estimators with different smoothing strategies will also be investigated to improve the accuracy and robustness of TF estimation. Moreover, field measurements will be conducted to further test the proposed methodology, both on straight tracks and curved tracks. The goal is to achieve track TF measurements at normal train operating speeds so that large-scale monitoring of track dynamic properties can be conducted efficiently.

CRediT authorship contribution statement

Yuanchen Zeng: Writing – review & editing, Writing – original draft, Validation, Methodology, Investigation, Formal analysis, Data curation, Conceptualization. **Alfredo Núñez:** Writing – review & editing, Supervision, Project administration, Methodology, Funding acquisition, Formal analysis. **Zili Li:** Writing – review & editing, Supervision, Resources, Project administration, Methodology, Funding acquisition, Conceptualization.

Declaration of competing interest

The authors declare that they have no known competing financial interests or personal relationships that could have appeared to influence the work reported in this paper.

Data availability

The data used to support the findings of this study are available from the corresponding author upon reasonable request.

Acknowledgment

The authors would like to thank Jan Moraal and Dr. Pan Zhang for their help in the laboratory measurements.

Funding

This research was partly supported by ProRail and Europe's Rail Flagship Project IAM4RAIL - Holistic and Integrated Asset Management for Europe's Rail System [grant agreement 101101966].

Appendix 1

The following derivation based on the time-domain method in [17] is presented below to support Eqs. (7)–(9) in Section 2.1.2. According to the Duhamel integral, the i-th modal displacement is expressed as follows.

$$q_i(t) = e^{-\omega_i\xi_i t}\left(\frac{\dot{q}_i(0)+\omega_i\xi_i q_i(0)}{\omega_{\mathrm{d}i}}\sin(\omega_{\mathrm{d}i}t)+q_i(0)\cos(\omega_{\mathrm{d}i}t)\right)+\frac{e^{-\omega_i\xi_i t}}{m_i^*\omega_{\mathrm{d}i}}\int_0^t e^{\omega_i\xi_i\tau}p_i(\tau)\sin(\omega_{\mathrm{d}i}(t-\tau))d\tau \tag{A1}$$

where $p_i(0)$ and $\dot{q}_i(0)$ are the initial modal displacement and velocity, respectively.

By taking the first-order and second-order derivatives of Eq. (A1) with respect to t, the modal velocity and acceleration can be obtained, respectively. Then, the modal displacement, velocity, and acceleration are discretized in the time step from s-1 to s ($\Delta t = t_s$-t_{s-1}, $s = 1, 2, \ldots$) as follows.

$$q_i(t_s) = e^{-\omega_i\xi_i\Delta t}\left(\frac{\dot{q}_i(t_{s-1})+\omega_i\xi_i q_i(t_{s-1})}{\omega_{\mathrm{d}i}}\sin(\omega_{\mathrm{d}i}\Delta t)+q_i(t_{s-1})\cos(\omega_{\mathrm{d}i}\Delta t)\right)+\frac{e^{-\omega_i\xi_i\Delta t}}{m_i^*\omega_{\mathrm{d}i}}\int_0^{\Delta t} e^{\omega_i\xi_i\tau}p_i(\tau)\sin(\omega_{\mathrm{d}i}(\Delta t-\tau))d\tau \tag{A2}$$

$$\dot{q}_i(t_s) = e^{-\omega_i\xi_i\Delta t}\left(\left(\dot{q}_i(t_{s-1})+\omega_i\xi_i q_i(t_{s-1})\right)\cos(\omega_{\mathrm{d}i}\Delta t)-\omega_{\mathrm{d}i}q_i(t_{s-1})\sin(\omega_{\mathrm{d}i}\Delta t)\right)+\frac{e^{-\omega_i\xi_i\Delta t}}{m_i^*\omega_{\mathrm{d}i}}\frac{\mathrm{d}}{\mathrm{d}t}\int_0^{\Delta t} e^{\omega_i\xi_i\tau}p_i(\tau)\sin(\omega_{\mathrm{d}i}(\Delta t-\tau))d\tau - \omega_i\xi_i q_i(t_s) \tag{A3}$$

$$\ddot{q}_i(t_s) = \left(\left(2\omega_i^2\xi_i^2 - \omega_i^2\right)\dot{q}_i(t_{s-1}) + \omega_i^3\xi_i q_i(t_{s-1})\right)\frac{e^{-\omega_i\xi_i\Delta t}\sin(\omega_{di}\Delta t)}{\omega_{di}} - \left(\omega_i^2 q_i(t_{s-1}) + 2\omega_i\xi_i\dot{q}_i(t_{s-1})\right)e^{-\omega_i\xi_i\Delta t}\cos(\omega_{di}\Delta t) + \frac{e^{-\omega_i\xi_i\Delta t}}{m_i^*\omega_{di}}\left(\omega_i^2\xi_i^2 - 2\omega_i\xi_i\frac{d}{dt} + \frac{d^2}{dt^2}\right)\int_0^{\Delta t} e^{\omega_i\xi_i\tau}p_i(\tau)\sin(\omega_{di}(\Delta t - \tau))d\tau \tag{A4}$$

The following integrals can be obtained when the modal force is assumed constant within the time step from s-1 to s.

$$\int_0^{\Delta t} e^{\omega_i\xi_i\tau}p_i(\tau)\sin(\omega_{di}(\Delta t - \tau))d\tau = \frac{p_i(t_{s-1})}{\omega_i^2}\left(\omega_{di}e^{\omega_i\xi_i\Delta t} - \omega_{di}\cos(\omega_{di}\Delta t) - \omega_i\xi_i\sin(\omega_{di}\Delta t)\right) \tag{A5}$$

$$\frac{d}{dt}\int_0^{\Delta t} e^{\omega_i\xi_i\tau}p_i(\tau)\sin(\omega_{di}(\Delta t - \tau))d\tau = \frac{p_i(t_{s-1})}{\omega_i}\left(\omega_{di}\xi_i e^{\omega_i\xi_i\Delta t} + \omega_i\left(1-\xi_i^2\right)\sin(\omega_{di}\Delta t) - \omega_{di}\xi_i\cos(\omega_{di}\Delta t)\right) \tag{A6}$$

$$\frac{d^2}{dt^2}\int_0^{\Delta t} e^{\omega_i\xi_i\tau}p_i(\tau)\sin(\omega_{di}(\Delta t - \tau))d\tau = p_i(t_{s-1})\left(\omega_{di}\xi_i^2 e^{\omega_i\xi_i\Delta t} + \omega_{di}\left(1-\xi_i^2\right)\cos(\omega_{di}\Delta t) + \omega_i\xi_i\left(1-\xi_i^2\right)\sin(\omega_{di}\Delta t)\right) \tag{A7}$$

Eqs. (7)–(9) can then be obtained by substituting Eqs. (A5)–(A7) to Eqs. (A2)–(A4).

References

[1] R.J. Allemang, R.S. Patwardhan, M.M. Kolluri, A.W. Phillips, Frequency response function estimation techniques and the corresponding coherence functions: a review and update, Mech. Syst. Sig. Process. 162 (2022) 108100.
[2] K. Knothe, Y. Wu, Receptance behaviour of railway track and subgrade, Arch. Appl. Mech. 68 (1998) 457–470.
[3] A.P. De Man, Dynatrack: a survey of dynamic railway track properties and their quality, Delft University of Technology, 2002.
[4] C. Shen, R. Dollevoet, Z. Li, Fast and robust identification of railway track stiffness from simple field measurement, Mech. Syst. Sig. Process. 152 (2021) 107431.
[5] Y. Zeng, C. Shen, A. Núñez, R. Dollevoet, W. Zhang, Z. Li, An interpretable method for operational modal analysis in time-frequency representation and its applications to railway sleepers, Struct. Control Health Monit. 2023 (2023) 6420772.
[6] H.F. Lam, M.T. Wong, Y.B. Yang, A feasibility study on railway ballast damage detection utilizing measured vibration of in situ concrete sleeper, Eng. Struct. 45 (2012) 284–298.
[7] M. Oregui, Z. Li, R. Dollevoet, Identification of characteristic frequencies of damaged railway tracks using field hammer test measurements, Mech. Syst. Sig. Process. 54 (2015) 224–242.
[8] M. Oregui, M. Molodova, A. Núñez, R.P.B.J. Dollevoet, Z. Li, Experimental investigation into the condition of insulated rail joints by impact excitation, Exp. Mech. 55 (2015) 1597–1612.
[9] N. Vincent, D.J. Thompson, Track dynamic behaviour at high frequencies. Part 2: experimental results and comparisons with theory, Veh. Syst. Dyn. 24 (sup1) (1995) 100–114.
[10] E. Berggren, Railway track stiffness: dynamic measurements and evaluation for efficient maintenance, KTH Royal Institute of Technology, 2009.
[11] P. Wang, L. Wang, R. Chen, J. Xu, J. Xu, M. Gao, Overview and outlook on railway track stiffness measurement, Journal of Modern Transportation 24 (2) (2016) 89–102.
[12] L. Wei, J. Zeng, P. Wu, C. Song, Safety analysis of high speed trains under cross winds using indirect wheel-rail force measuring method, J. Wind Eng. Ind. Aerodyn. 183 (2018) 55–67.
[13] P. Urda, S. Muñoz, J.F. Aceituno, J.L. Escalona, Wheel-rail contact force measurement using strain gauges and distance lasers on a scaled railway vehicle, Mech. Syst. Sig. Process. 138 (2020) 106555.
[14] F. Xia, C. Cole, P. Wolfs, Grey box-based inverse wagon model to predict wheel–rail contact forces from measured wagon body responses, Veh. Syst. Dyn. 46 (S1) (2008) 469–479.
[15] S. Pourzeynali, X. Zhu, A. Ghari Zadeh, M. Rashidi, B. Samali, Comprehensive study of moving load identification on bridge structures using the explicit form of newmark-β method: Numerical and experimental studies, Remote Sens. (Basel) 13 (12) (2021) 2291.
[16] Wu, J., Zhu, T., Wang, Y., Lei, C., Xiao, S. (2022). TSVD regularization-parameter selection method based on Wilson-θ and its application to vertical wheel-rail force identification of rail vehicles. Shock and Vibration, 2022.
[17] T. Zhu, X.R. Wang, Y.W. Fan, M.M. Wang, J.K. Zhang, S.N. Xiao, B. Yang, A time domain method for wheel-rail force identification of rail vehicles, Veh. Syst. Dyn. 60 (3) (2022) 790–809.
[18] P. Lutzmann, B. Göhler, F. Van Putten, C.A. Hill, Laser vibration sensing: overview and applications, Electro-Optical Remote Sensing, Photonic Technol., Appl. V 8186 (2011) 11–26.
[19] S.J. Rothberg, M.S. Allen, P. Castellini, D. Di Maio, J.J.J. Dirckx, D.J. Ewins, J.F. Vignola, An international review of laser doppler vibrometry: making light work of vibration measurement, Opt. Lasers Eng. 99 (2017) 11–22.
[20] Y. Zeng, A. Núñez, Z. Li, Speckle noise reduction for structural vibration measurement with laser doppler vibrometer on moving platform, Mech. Syst. Sig. Process. 178 (2022) 109196.
[21] E.J. OBrien, A. Malekjafarian, A mode shape-based damage detection approach using laser measurement from a vehicle crossing a simply supported bridge, Struct. Control Health Monit. 23 (10) (2016) 1273–1286.
[22] K. Kaynardag, G. Battaglia, A. Ebrahimkhanlou, A. Pirrotta, S. Salamone, Identification of bending modes of vibration in rails by a laser doppler vibrometer on a moving platform, Exp. Tech. 45 (1) (2021) 13–24.
[23] K. Kaynardag, C. Yang, S. Salamone, A rail defect detection system based on laser doppler vibrometer measurements, NDT and E Int. 102858 (2023).
[24] Y. Jin, R. Dollevoet, Z. Li, Numerical simulation and characterization of speckle noise for laser doppler vibrometer on moving platforms (LDVom), Opt. Lasers Eng. 158 (2022) 107135.
[25] Y. Zeng, A. Núñez, Z. Li, Railway sleeper vibration measurement by train-borne laser doppler vibrometer and its speed-dependent characteristics, Comput. Aided Civ. Inf. Eng. (2024).
[26] Y. Zeng, A. Núñez, Z. Li, A simulation study on characterizing transfer functions of railway tracks using train-borne laser doppler vibrometer, in: International Conference on Experimental Vibration Analysis for Civil Engineering Structures, Cham, Springer Nature Switzerland, 2023, pp. 183–192.
[27] R. Brincker, L. Zhang, P. Andersen, Modal identification of output-only systems using frequency domain decomposition, Smart Mater. Struct. 10 (3) (2001) 441.
[28] R. Brincker, C.E. Ventura, P. Andersen, Damping estimation by frequency domain decomposition, in: In Proceedings of IMAC 19: A Conference on Structural Dynamics. Society for Experimental Mechanics, 2001, pp. 698–703.

[29] P. Welch, The use of fast fourier transform for the estimation of power spectra: a method based on time averaging over short, modified periodograms, IEEE Trans. Audio Electroacoust. 15 (2) (1967) 70–73.
[30] C. Rainieri, G. Fabbrocino, Operational modal analysis of civil engineering structures, Springer, New York, 2014, pp. 103–210.
[31] L. Ljung, On the estimation of transfer functions, Automatica 21 (6) (1985) 677–696.
[32] Broersen, P. M. (1994). A comparison of transfer function estimators. In Conference Proceedings. 10th Anniversary. IMTC/94. Advanced Technologies in I & M. 1994 IEEE Instrumentation and Measurement Technolgy Conference. IEEE; 1377-1380.
[33] A. Stenman, F. Gustafsson, D.E. Rivera, L. Ljung, T. McKelvey, On adaptive smoothing of empirical transfer function estimates, Control Eng. Pract. 8 (11) (2000) 1309–1315.
[34] J. Lataire, T. Chen, Transfer function and transient estimation by gaussian process regression in the frequency domain, Automatica 72 (2016) 217–229.
[35] M. Naeimi, Z. Li, R.H. Petrov, J. Sietsma, R. Dollevoet, Development of a new downscale setup for wheel-rail contact experiments under impact loading conditions, Exp. Tech. 42 (2018) 1–17.